



Contents lists available at ScienceDirect

Journal of Rock Mechanics and Geotechnical Engineering

journal homepage: www.jrmge.cn

Full Length Article

Crack and failure behaviors of sandstone subjected to dynamic loads visualized by micro-computed tomography

Xingyu Zhang^{a, b, c}, Pengfei Guo^d, Xiangbo Gao^b, Chunjiang Zou^e, Kaiyu Wang^b,
Jinzhu Hu^d, Yan Sun^d, Liang Lei^{a, b, c, *}

^a Institute of Advanced Technology, Westlake Institute for Advanced Study, Hangzhou, 310024, China

^b Key Laboratory of Coastal Environment and Resources of Zhejiang Province, School of Engineering, Westlake University, Hangzhou, 310030, China

^c Research Center for Industries of the Future, Westlake University, Hangzhou, 310030, China

^d Key Laboratory of Rock Mechanics and Geohazards of Zhejiang Province, Shaoxing University, Shaoxing, 312000, China

^e Department of Civil and Environmental Engineering, Brunel University, London, UB8 3PH, United Kingdom

ARTICLE INFO

Article history:

Received 29 December 2023

Received in revised form

21 March 2024

Accepted 14 May 2024

Keywords:

Dynamic rock failure

3D observation

Microscopic failure mechanism

ABSTRACT

Microscopic dynamic failure behaviors of rocks are significant to rock engineering, which is still insufficiently understood. This study combines split Hopkinson pressure bar (SHPB) and micro-CT (computed tomography) to explore the microscopic failure characteristics of sandstone under impact loading. SHPB is responsible for the dynamic test, and micro-CT is responsible for pre- and post-test inspections. The results show that the pores and defect influence the dynamic strength but do not alter the overall trend of increased strength with a higher impact level. The dynamical crack development is then analyzed. Three types of cracks (i.e. I-, Y-, and H-type) are identified to describe the crack development. When rock is simply fractured, only I-type crack exists due to tensile failure, and it grows irregularly. As the strain rate increases, I-type crack is transformed into Y- and H-type crack due to shear failure. Crack coalesces at that moment, and the complexity increases along the impact direction. The coalescence occurs preferentially in the area with more pores, and around a third of pores are involved, where the maximum contribution area is in the middle of sample. Microcracks are formed inside the rock blocks, and rock grains and fragments fill in the cracks. The dynamic crack development is accompanied by microcracks, while rock grains and fragments result from the development of these microcracks. In addition, the influence of a semi-penetrating defect perpendicular to the impact direction is investigated. The defect can impede stress transfer and concentrate energy consumption. The findings are expected to enhance understanding of rock dynamics and support rock engineering development.

© 2024 Institute of Rock and Soil Mechanics, Chinese Academy of Sciences. Production and hosting by Elsevier B.V. This is an open access article under the CC BY-NC-ND license (<http://creativecommons.org/licenses/by-nc-nd/4.0/>).

1. Introduction

The dynamic behavior of rock is vital in rock engineering. Understanding the dynamic behavior of rock is crucial in many engineering disciplines, such as tunneling, mining, and slope engineering, as it contributes to predicting the response of rock to dynamic loading and reducing the risk of engineering failure (Zhao and Li, 2013). However, rock in nature is inherently heterogeneous

and discontinuous, which makes its dynamic behavior complex (Austrheim et al., 2017). Many studies have been conducted on dynamical failure characteristics and mechanisms of rock. Li et al. (2013; 2017a) used the split Hopkinson pressure bar (SHPB) to study the dynamic response and failure mechanism of sandstone. Gong et al. (2019) investigated dynamic mechanical properties and failure characteristics of sandstone with low confining pressure by a modified SHPB test. Wang et al. (2016) analyzed the damage evolution of impacted sandstone after freeze-thaw cycles based on the SHPB test. Rock failure characteristics and mechanisms are typically studied with regard to stress and environmental conditions, and the SHPB test is commonly used.

Microscopic failure characteristics and mechanisms have recently attracted more attention. Li et al. (2017b) established a

* Corresponding author. Institute of Advanced Technology, Westlake Institute for Advanced Study, Hangzhou, 310024, China.

E-mail address: Leiliang@westlake.edu.cn (L. Lei).

Peer review under responsibility of Institute of Rock and Soil Mechanics, Chinese Academy of Sciences.

<https://doi.org/10.1016/j.jrmge.2024.05.001>

1674-7755/© 2024 Institute of Rock and Soil Mechanics, Chinese Academy of Sciences. Production and hosting by Elsevier B.V. This is an open access article under the CC BY-NC-ND license (<http://creativecommons.org/licenses/by-nc-nd/4.0/>).

grain-based sandstone model by high-resolution scan and image processing, and then tested the model via the discrete element method to mimic the SHPB test. Zhou et al. (2019) employed digital image correlation (DIC) incorporated with SHPB to study the dynamic response and failure pattern of sandstone with different prestresses. Wang et al. (2022) utilized a combination of high-speed photography, scanning electron microscope (SEM), and DIC techniques with the SHPB test to study the crack growth and failure mechanism of sandstone. The development of image monitoring and processing techniques facilitates the study of the microscopic and dynamic failure characteristics of rock. Microscopic research enriches and enhances the understanding of rock's dynamic failure. However, these studies only utilize surface observation via techniques such as DIC and SEM, so internal and 3D (three-dimensional) failure characteristics are missing, especially when the rock breaks apart upon the occurrence of macroscopic failure.

Micro-CT is a promising technique that enables both 3D nondestructive visualization and high-precision imaging, and its application is emerging in rock dynamics. Huang et al. (2013) used a modified SHPB system and micro-CT to observe the microscopic damage accumulation of rock under dynamic compressive loading. Yao et al. (2020) further examined the damage evolution and the fracture features in the microscopic view while rock was subjected to different loading rates and strain levels. Liu et al. (2019, 2020b) studied the crack network and failure pattern of rock under triaxial stress conditions with the help of synchrotron-based micro-CT. These works pioneer the use of micro-CT to understand the rock dynamic behavior from the 3D view. However, aided by micro-CT, the existing research only focuses on the dynamic crack development after the impact, which may overlook other information, such as the fractured characteristics of rock blocks. In addition, rock is inherently heterogeneous and discontinuous, so the initial features possibly affect the dynamic failure. The existing works did not conduct the pre-scanning and thus failed to consider the initial structure influence of rock, such as pores and defect.

In this context, we studied the microscopic failure characteristics of sandstone under impact loading. By combining SHPB and micro-CT, the dynamic behavior, internal crack propagation, and fractured block characteristics are revealed from the microscopic view. The dynamic failure behavior and influence of initial structures are discussed. Some insights are provided to guide safe construction and disaster prevention in various engineering.

2. Method

The test procedures and methods are illustrated in Fig. 1. As shown in Fig. 1a, the sandstone samples were prepared according to requirements of SHPB test. First, the samples were scanned by micro-CT, and the interior characteristics of original samples were obtained. Then the samples were impacted by SHPB, and the dynamic properties of rock were obtained. After the SHPB test, the interior characteristics of rock would change. Micro-CT was used again to obtain the sample interior characteristics. Finally, the microscopic failure characteristics of sandstone under impact loading were identified by comparing micro-CT test results before and after SHPB tests.

X-ray CT is a nondestructive imaging technique to observe the interior 3D structure of an object. As shown in Fig. 1b, the micro-CT uses X-ray to produce magnified images of the object. Various substances in the object have different X-ray attenuation coefficients, making them distinguishable. The magnification is the ratio of focus-to-detector distance (FDD) to focus-to-object distance (FOD) according to geometric magnification. The sample is attached to a holder. ZEISS Xradia 610 Versa is used in this study to visualize the microscopic characteristics of the sample.

A classical SHPB system was used in this study, as shown in Fig. 1c. Table 1 lists the parameters of the SHPB device. The strain gauge on the incident bar measures the incident wave strain and the reflected wave strain in succession, and the strain gauge on the transmitted bar measures the transmitted wave strain. Wheatstone bridge circuits can accurately measure the minimal signal. A high dynamic strain indicator is used to amplify the signals so that the oscilloscope records the short-duration signal. According to the three-wave method, based on the one-dimensional wave propagation theory, the dynamic stress-strain relation is obtained by

$$\left. \begin{aligned} \varepsilon &= \frac{C_B}{L_S} \int_0^t (\varepsilon_I - \varepsilon_R - \varepsilon_T) dt \\ \sigma &= \frac{1}{2} \frac{A_B}{A_S} E_B (\varepsilon_I + \varepsilon_R + \varepsilon_T) \end{aligned} \right\} \quad (1)$$

where σ and ε are the dynamic compressive stress and strain of the sample, respectively; C_B , A_B and E_B are the wave velocity, cross-sectional area, and elastic modulus of bars, respectively; L_S and A_S are the length and cross-sectional area of the sample, respectively; and ε_I , ε_R and ε_T are the strain signals of the incident, reflected and transmitted wave, respectively.

3. Sample material and test preparation

3.1. Sandstone characterization

The sandstone for test was collected from an underground coalmine in Henan Province, China. The average mining depth was 700 m. We extracted the sandstone from the roof of roadway at the excavation front, preventing the sandstone from excessive subsequent disturbances, such as mining or roadway maintenance activities. The extracted bulk sandstone was then carefully cut into cylindrical samples for SHPB tests. The sample preparation refers to the International Society for Rock Mechanics and Rock Engineering (ISRM) suggestion on rock dynamic tests and relevant studies for the SHPB test with sandstone (Dai et al., 2010; Zhou et al., 2012; Liang et al., 2015). The cylindrical sandstone sample has a radius of 50 mm, and the aspect ratio is set as 0.8. The flatness and perpendicularity of the sides are well controlled within a tolerance of ± 0.05 mm and $\pm 0.25^\circ$, respectively. Petrographic characteristics of sandstone are important for the mechanical property. The micro-CT scan was first conducted with the cylindrical sample. As shown in Fig. 2a, the 3D features are described graphically. Substances with different attenuation coefficients are depicted in gray values ranging from 0 to 255. The brightness or intensity of voxels decreases as the density of minerals decreases from high to medium and eventually to the pores depicted in black. The micro-CT image resolution varies slightly at around 27 μm .

Then thin sections of rock samples were analyzed to identify the composition of the sandstone. Under the polarizing microscope, as shown in Fig. 2b, the sandstone consists of debris and interstitial fillings. Through the measurement and identification, the 68% debris comprises 61% quartz, 5% feldspar, and 2% mica; the 32% interstitial fillings consist of 16% siderite, 8% calcite, and 8% silicon. Combined with the micro-CT test results, the main mineral in the white domain is the interstitial filling of siderite according to the mineral density and composition. In contrast, the minerals in the gray domain consist of a mixture of debris (quartz and feldspar) and interstitial fillings (calcite and silicon), in which debris dominates with a percentage of 80.5%. Fig. 2c shows the sandstone morphological features obtained by SEM. The sandstone has clear cementation. Pores mainly appear in the interstitial fillings. These characterizations facilitate the segmentation of micro-CT images as

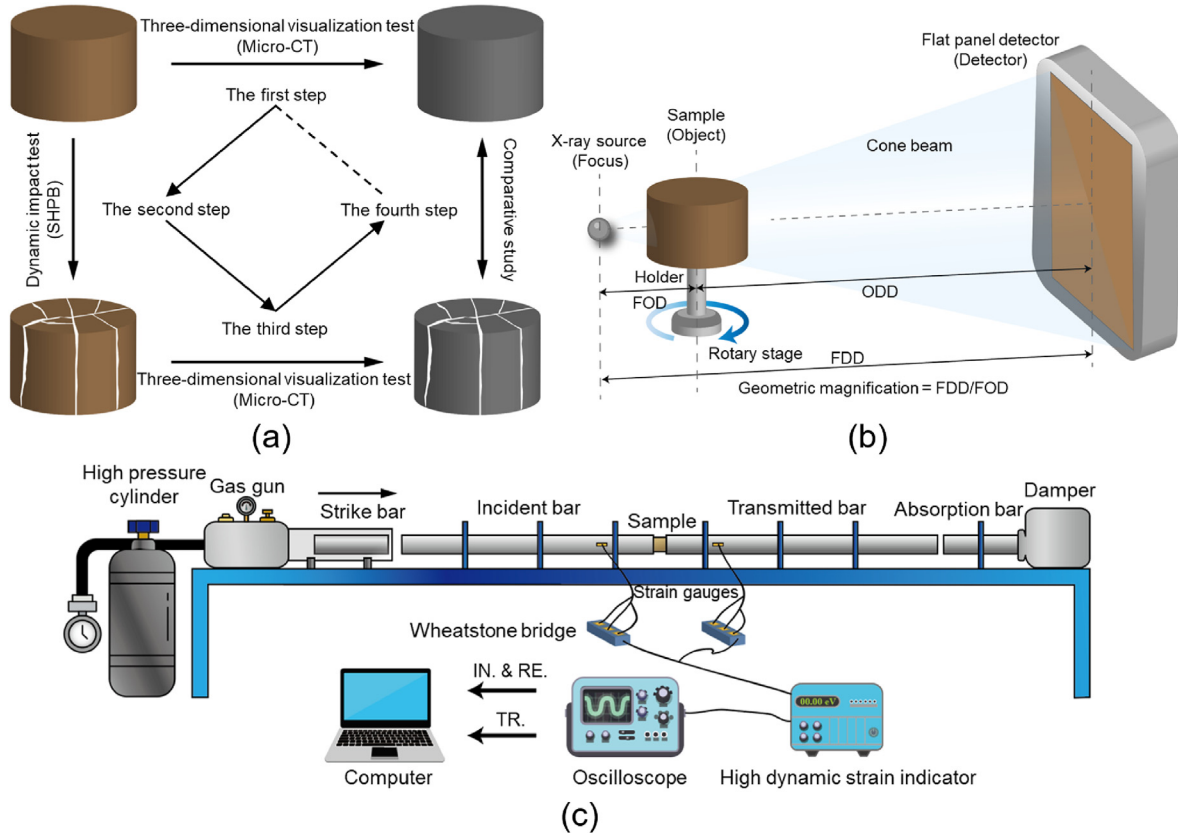


Fig. 1. Test procedures and methods. (a) Schematic of test procedures, (b) basic principle of X-ray micro-CT, and (c) schematic of SHPB test system.

Table 1
Geometrical and mechanical parameters of the used SHPB device.

Parameters	Value
Length of strike bar (mm)	600
Length of incident bar (mm)	5000
Length of transmitted bar (mm)	3000
Diameter of bars (mm)	75
Density of bars (kg/m ³)	7800
Young's modulus (GPa)	200
Distance from strain gauge to incident end of sample (mm)	1200
Distance from strain gauge to transmitted end of sample (mm)	800
Stress wave velocity in bars (m/s)	5160

well as the following analysis of the microscopic dynamic failure of sandstone.

In this context, we employed the ilastik software based on the interactive supervised machine learning approach (Berg et al., 2019). The supervised machine learning method has been justified to be capable of accurately segmenting rock material from X-ray CT images (Purswani et al., 2020; Reinhardt et al., 2022). Additionally, an emerging method of RockSAM shows good potential for effectively segmenting rock material (Ma et al., 2023a, 2023b). As shown in Fig. 3, three categories of high-density minerals, background minerals, and pores are identified based on the micro-CT scan results. According to the SEM and thin-section observations, the predominant mineral is the interstitial filling of siderite in the high-density minerals while the debris is predominant in the background minerals. The pores are mainly located around siderite, and the sizes of visible pores herein are larger than the image resolution.

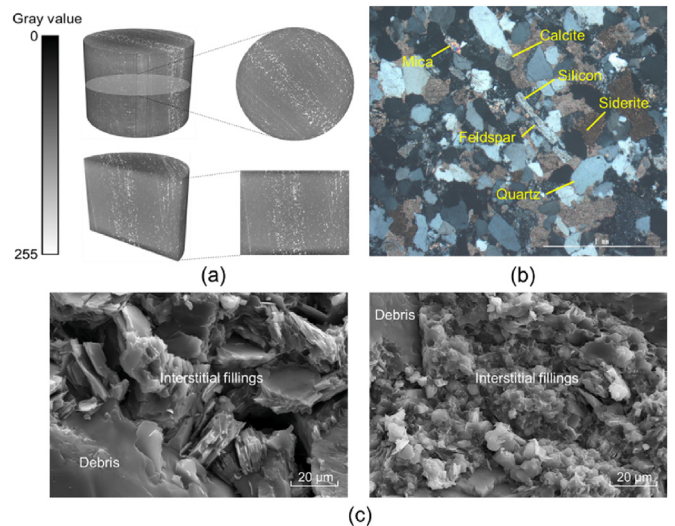


Fig. 2. Micrographs of sandstone. (a) Micro-CT 3D imaging, (b) polarized thin-section imaging, and (c) SEM images.

3.2. Test scheme

The dynamic stress equilibrium state was first inspected. The sample was sandwiched between the 2 bars, and lubricating grease was spread to minimize friction on the contact surfaces. Stresses on both ends of the sample were compared under the SHPB test with a high strain rate. Stresses on the incident end (σ_1) and the transmitted end (σ_2) can be calculated by

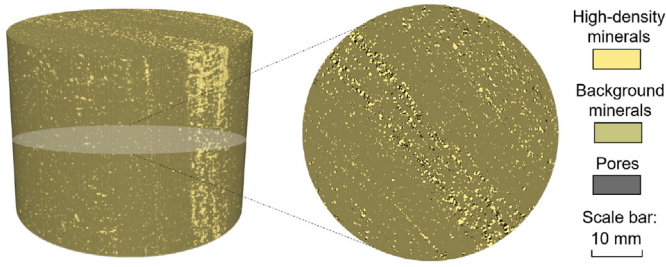


Fig. 3. Segmentation and construction of 3D rock sample.

$$\left. \begin{aligned} \sigma_1 &= \frac{A_B}{A_S} E_B (\epsilon_1 + \epsilon_R) \\ \sigma_2 &= \frac{A_B}{A_S} E_B \epsilon_T \end{aligned} \right\} \quad (2)$$

where σ_1 is represented by the green and σ_2 by the red dot line (see Fig. 4). The two lines match well. Therefore, the inertial effect of the sample can be ignored during the SHPB test, validating the test's rationality.

Next, different levels of impact are set to study the microscopic failure behavior of the sandstone. According to Doan and Gary (2009), three impact levels of low, intermediate, and high strength are defined according to final states of the samples. They are the unbroken, simple fracturing, and multiple fragmentation states. Based on the test method (see Fig. 1a), six sandstone samples were paired up with three impact levels.

4. Results

4.1. Mechanical behavior and internal structure visualization

The dynamic stress-strain relation of the samples is shown in Fig. 5. The general trend shows that the dynamic strength increases significantly with a rise in the impact level, which matches the existing research results (e.g. Luo et al., 2020; Mishra et al., 2020). However, some differences are noteworthy. Under the low impact, the two curves are comparable, and the dynamic strengths are close. However, the curve disparity becomes noticeable as the impact level increases although the two samples were subjected to the same impact level.

To quantify the differences, the dynamic physicommechanical

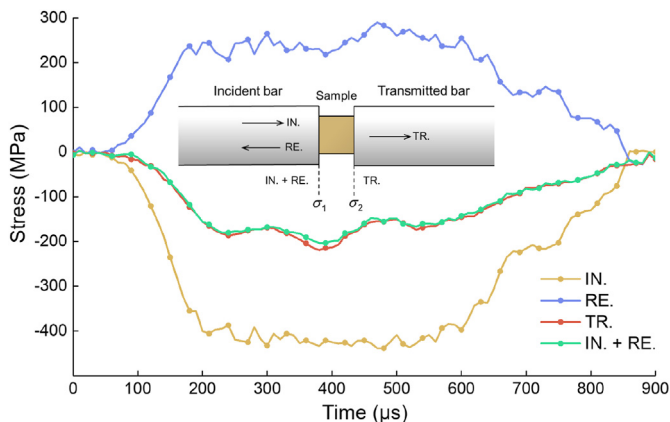


Fig. 4. Dynamic stresses on both ends of the sample. IN., RE., and TR. represent the incident, reflected, and transmitted stress, respectively.

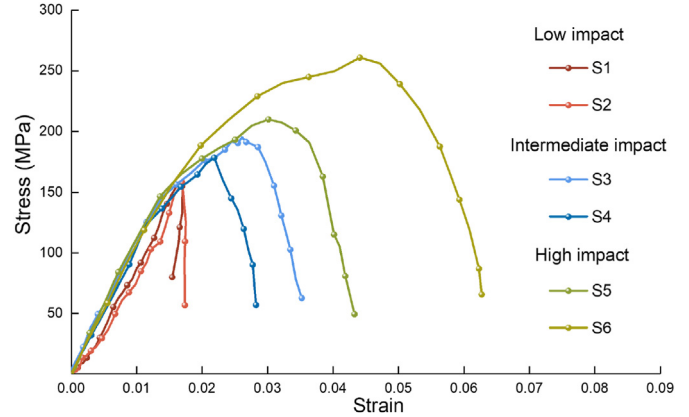


Fig. 5. Dynamic stress-strain curves of six samples.

properties of the samples are summarized in Table 2. The dynamic modulus is determined by an approximate linear segment in the first half of stress-strain curves. As the strain rate increases, the dynamic modulus does not follow the same trend as the peak strength and strain. In addition, the peak strength and strain do not continuously increase with the increase in strain rate. As shown in Fig. 6, under the intermediate impact, the strain rate of S4 is obviously greater than that of S3, but the peak strength and peak strain are smaller. When it comes to the high impact, the strain rate of S6 is only slightly greater than that of S5, but there is a substantial increase in both the peak strength and strain.

In rock dynamics, the peak strength of rock typically increases as the strain rate increases, while the peak strength of S4 with a clearly larger strain rate is less than the peak strength of S3. In conventional tests, the rock samples are intervened by testing the wave velocity, and the samples with similar wave velocities are selected, so the rock heterogeneity is minimized as possible during SHPB tests. We herein purposely skipped the wave velocity test in the sample preparation stage to investigate the potential effects of heterogeneity. Aided by micro-CT tests, the 3D visualization and quantification can help explain the results. As shown in Fig. 7, the internal pores were extracted. Fig. 7a shows the 3D morphology of pores in S3. The pore volume of S3 is 1.71 cm³, which is similar to other cases except for S4 and S5. As for S4 shown in Fig. 7b, more pores are observed than that of S3, and the volume is 3.21 cm³, which is nearly twice as much. According to the study of dynamics on brittle material, the presence of pores reduces the contact area between the particles and matrix, weakening the mechanical integrity of the host material (Katcoff and Graham-Brady, 2014). Previous studies (e.g. Changani, 2015; Emad et al., 2023), to some extent have highlighted that the higher porosity in rocks can reduce their dynamic strength. Therefore, the high volume of pores is most likely the cause of the decrease in dynamic strength, although the strain rate increases. The strain rate of S5 is around 6.6% lower than that of S6, but the dynamic strength is significantly lower by 19.5%, with a difference of more than 50 MPa. This is because a semi-penetrating native defect exists in S5, as shown in Fig. 7c. The total volume of black domains (pores and the defect) in S5 is 1.08 cm³, less than that of S3 (1.71 cm³), but S5 has lower compression resistance because of the transverse defect. It is noteworthy that neither the pores nor the defects change the fact that the dynamic strength increases with the rise of impact level. It is important to note that the sandstone samples had different pore distributions under micro-observations, indicating the inherent heterogeneity of rock. According to the characterizations in Section 3.1, the distribution and content of the high-density minerals, to some extent,

Table 2
Dynamic physicochemical properties of the samples.

Sample	Impact level	Gas pressure, P (MPa)	Strain rate, $\dot{\epsilon}$ (s^{-1})	Peak strength, σ_d (MPa)	Peak strain, ϵ_d	Dynamic modulus, E_d (GPa)
S1	Low	0.15	82.39	158.24	0.016	10.57
S2			83.39	157.80	0.017	10.75
S3	Intermediate	0.20	105.37	195.27	0.026	10.32
S4			125.53	178.40	0.022	10.80
S5	High	0.25	158.44	209.97	0.030	11.02
S6			168.88	260.91	0.044	10.15

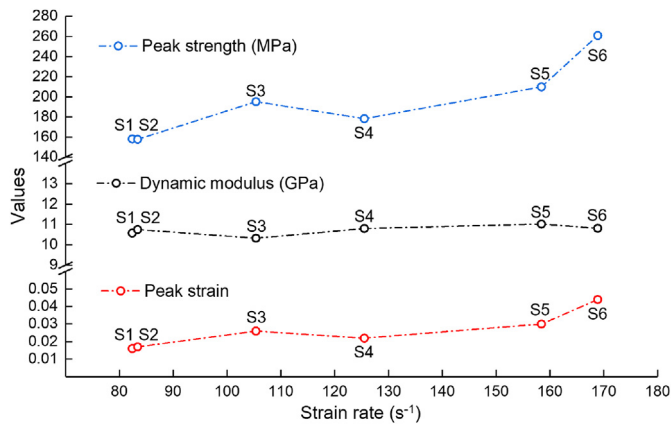


Fig. 6. Dynamic properties change with increase of the strain rate.

determine the spatial distribution of pores in the sample.

4.2. 3D characteristics of crack propagation

After the SHPB tests, the micro-CT re-scanned the samples to identify the 3D characteristics of crack propagation. The samples subjected to low impact remained intact without clear cracks forming, as observed in comparing results before and after the impact loading. In addition, S6 was severely damaged due to the high strain rate and cannot be recovered. Therefore, representative samples of S3, S4, and S5 were collected to demonstrate the dynamic crack propagation, as shown in Fig. 8. The upper and lower half display the 3D pattern and the top view, in which the impact comes from the top.

The sample was fractured as the impact leveled up to the intermediate. As shown in Fig. 8a, the crack is only developed in the axial direction, taking the T-shape. With increase in the strain rate, as shown in Fig. 8b, branches are derived from the dominant crack and cracks are coalesced. The coalescence was developed not only in the axial but also in the radial direction. Overall, the crack propagation was mainly simple fracturing with localized

coalescence. Compared to the sample before SHPB, it is apparent that the coalescence is primarily located where more pores pre-exist. As the strain rate continued to increase, crack propagation fundamentally changed. As shown in Fig. 8c, coalescence occurs globally. The crack propagation was rather complicated, presenting a state of multiple fragmentations, and the crack morphology was like a net. Compared to the sample before SHPB, it is noteworthy that the semi-through native defect propagates to a crack plane across the sample. Further, the crack propagation beneath the plane differed from the upper part. The case in the lower part was closer to that of S4 (see Fig. 8b). This phenomenon indicated that the strain rate in the lower part was significantly decreased. A crack perpendicular to the impact direction impeded the stress transfer.

4.3. Microscopic characteristics of fractured block

The characteristics of fractured blocks were further observed. Samples S3, S4, and S5 are put together for a comparative study, as shown in Fig. 9. Fig. 9a shows that S3 is split into several intact blocks. The long penetrating crack did not fracture along the bedding orientation of interstitial fillings while the derived crack showed the bedding-orientation dependency. In addition, as shown in the enlarged area A, a few rock grains were found in the crack. Meanwhile, although intergranular and transgranular fractures were found, the primary fracture was intergranular.

As shown in Fig. 9b, the number of blocks significantly increases when the strain rate increases. At an intermediate impact level, crack coalescence was confined to a specific area, leading to a significant variation in block size. Additionally, the rock grain and the rock fragment were formed in the crack. Rock grains and fragments filled in the crack increased both in size and quantity, as shown in the enlarged area B. Microcracks were developed in some blocks, as evidenced in the enlarged area C. The phenomena can be explained in view of energy. In the case of sample S3, the input energy was limited and totally dissipated by the dominant crack. When the energy was increased, the extra energy was dissipated by forming new cracks. However, the additional energy was limited during the intermediate impact. As a result, only some microcracks were formed, and the energy was dissipated before the cracks became obvious.

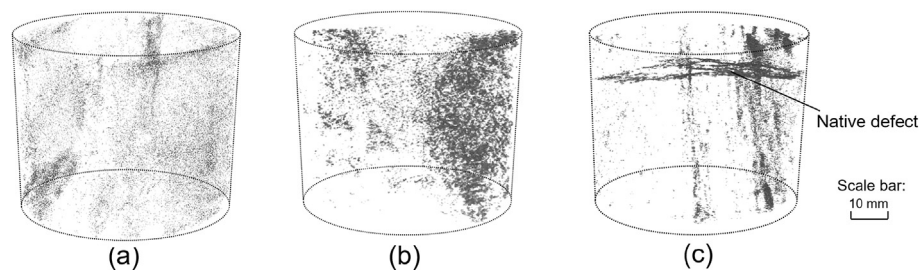


Fig. 7. 3D visualization of pores. (a) S3, (b) S4, and (c) S5.

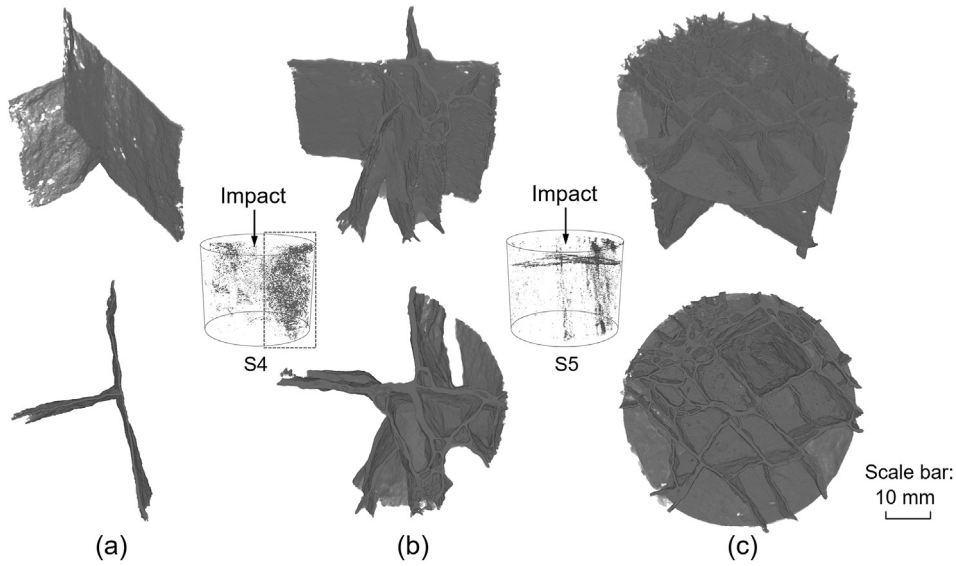


Fig. 8. Representative 3D characteristics of crack propagation. (a) S3, (b) S4, and (c) S5.

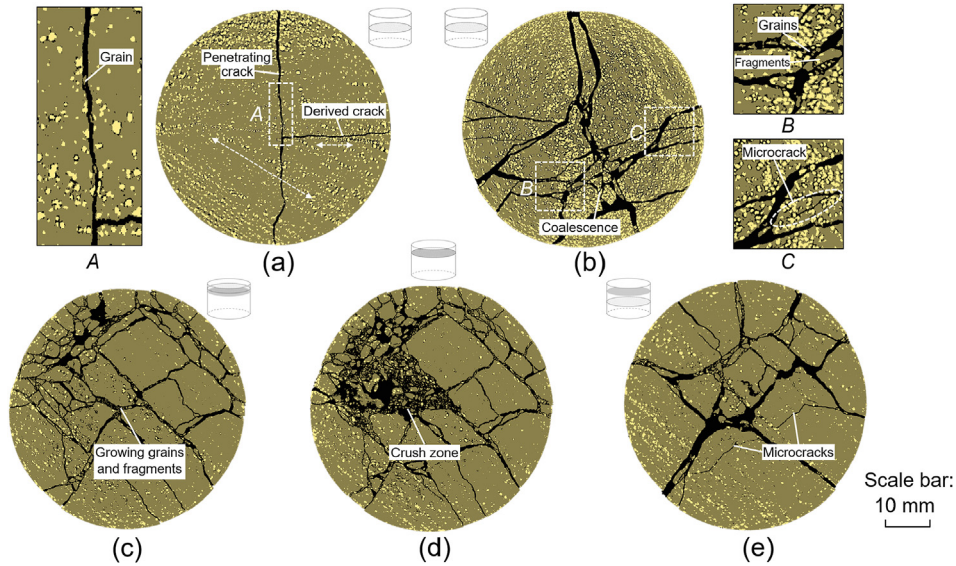


Fig. 9. Block fracture characteristics in the plan view. (a) S3, (b) S4, (c) S5 slice above the defect, (d) S5 slice at the defect, and (e) S5 slice below the defect.

When the strain rate is further increased, the high impact increases the block number, as shown in Fig. 9c. Compared to the case of S4, the difference in block size decreased due to the spreads of crack coalescence. The number of rock grains and fragments increased significantly, and the fragments were mainly small. In the state of multiple fragmentations, cracks were fully developed. Microcracks were not easy to catch in contrast. In addition, the native defect affected the block fracture characteristics. Fig. 9d shows the block fracture characteristics at the defect. Compared with Fig. 9c, the marked difference was the presence of a crush zone, in which rock was smashed into numerous grains. Fig. 9e shows the block fracture characteristics below the defect. The features are close to that of S4, as shown in Fig. 9b. The crack coalescence occurred locally, and microcracks appeared in the blocks. As illustrated in Section 4.2, the native defect impedes the stress transfer. Moreover, the crush zone helps consume the impact energy.

5. Discussion

5.1. Crack type

3D visualization enables the analyses of crack pattern inside the sample after dynamic failure. Three crack types are identified by observing crack planes along the loading direction: I-, Y-, and H-type, as depicted in Fig. 10. When the sample is simply fractured, the I-type crack emerges first. As shown in Fig. 10a, σ_1 is the principal stress under the impact condition. Due to the absence of confining stress, the rock sample tends to fail due to induced tension caused by Poisson's effect, as the dynamic tensile strength of rocks is significantly smaller than their dynamic compressive strength (Liu et al., 2018; Misa and Nowakowski, 2021; Padmanabha et al., 2023). The impact was not high, so the input energy was quickly consumed by forming several I-type cracks. When the impact level increased, the input energy was too high to

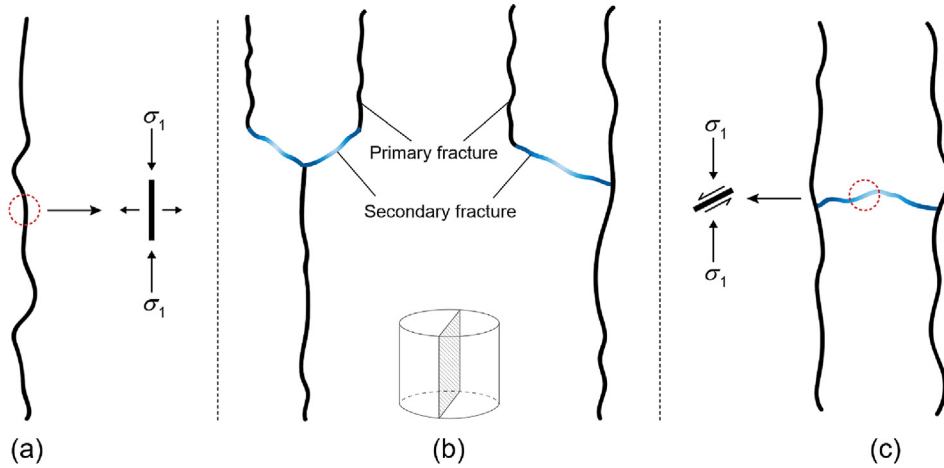


Fig. 10. Dynamic crack types and fracture mechanism from the vertical cross-section. (a) I-type, (b) Y-type, and (c) H-type.

be consumed by a few I-type cracks, and more cracks were therefore formed until a new equilibrium state was reached.

Interestingly, the cracks were not all I-type, although the rock exhibits the weakest strength in tension. Results showed coalescence occurred among cracks, which resulted in Y- and H-type cracks, as shown in Fig. 10b and c. The insight is a transition from the I-type to the Y- and H-type due to the secondary fracture. I-type crack was formed first and was primary in this case. As I-type cracks propagated, the stress field near the fracture changed and thus influenced the tendency of following crack development. In the limited space, not all potential cracks can develop in I-type. Secondary fractures occurred as coalescence cracks among I-type cracks, mainly driven by local shear stress. According to the relative positions between the primary and secondary fracture, crack type can be categorized into Y- and H-type. The Y-type crack includes the uppercase and lowercase y-shaped, as shown in Fig. 10b. The difference lies in whether the axial crack is fully or partially developed.

In real cases, crack morphology may include all three type cracks. When the coalescence does not occur, the crack is I-type and can be easily identified from S3. When the coalescence happens, the I-type crack is transformed into a combination of Y- and H-type. For example, cracks in sample S4 are shown in Fig. 11. Two slices of A and B were extracted, and only cracks were depicted. Y- and H-type cracks were formed based on I-type cracks. Meanwhile, the confined space of crack development limited a further development of Y- and H-type cracks due to the boundary effect. Although the actual situation is complicated because of the rock

heterogeneity, it may cause cracks not to appear in perfect shapes of “I,” “Y,” and “H.” However, three crack types can still be identified based on the above analysis.

5.2. Crack development mechanism

Observing crack development characteristics in the impact direction is vital to understanding crack growth behavior. Fig. 12 shows the variation of fractal dimension of crack in the slice, as observed along the impact direction. The algorithm adopts the classic box-counting method (Falconer, 2007). The dimension D is defined as

$$D = \lim_{\epsilon \rightarrow 0} \frac{\log_{10} N(\epsilon)}{\log_{10}(1/\epsilon)} \quad (3)$$

where $N(\epsilon)$ is the number of boxes of side length ϵ required to cover the set.

The 2D definition is used herein, and the results can indicate the roughness and complexity of cracks. As shown in the trend of S3, the fractal dimension increased stepwise. During the first three-quarter part, the fractal dimension basically kept stable with an average value of 1.088. Then the fractal dimension stepped to 1.134 on average with a leap. In contrast, the fractal dimension of S4 showed a gradual increase as the slice number increased, and the average value was about 1.266. Apparently, crack expansion and coalescence under a higher impact led to a greater fractal dimension, and their crack development differed for these samples.

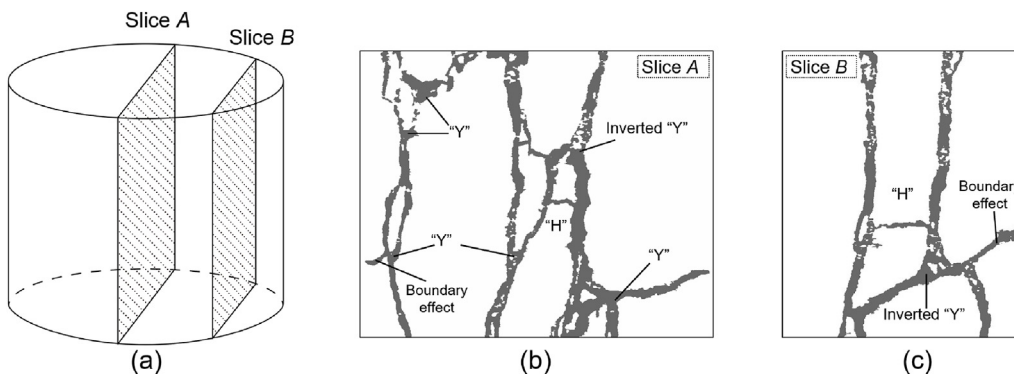


Fig. 11. Plan view of cracks in S4 after impact loading.

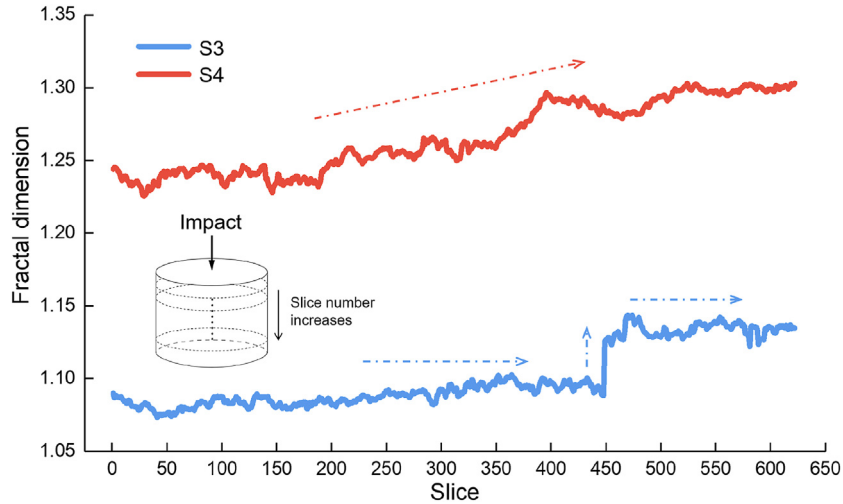


Fig. 12. Fractal dimension of crack along cross-section as the slice number changes. The dashed arrows in the diagram signify the varying trend observed in the solid lines.

To understand crack development, the variation of crack cross-sectional area was computed as the slice number changes. Crack complexity is related to its fractal dimension, and the complexity refers to as the intricacy of the crack pattern, including its branching and interconnection with other cracks (Saouma et al., 1990; Wen and Cheong, 2021). Therefore, an increase in the fractal dimension lies in the increased crack complexity. Crack roughness refers to as the irregularities on the surface of a crack, quantified by metrics describing its geometry. The complexity of cracks has a positive correlation with both the crack area and crack roughness (Brown, 1987; Brown and Liebovitch, 2010). These relationships are critical for understanding crack propagation mechanisms, indicating how cracks interact with the rock material and react under external dynamic loadings (Xie et al., 1997; Sun et al., 2021). As shown in Fig. 13, representative crack morphology regarding the fractal dimension was also posted at different stages. As the slice number increased, the crack area of S3 fluctuated within a narrow range. Even though the fractal dimension increased, the trend was not changed. The result indicates that the I-type crack growth is irregular though it is a single fracture. Along the impact direction, the I-type crack grows with an increase in its roughness, as compared in between the representative slices.

It can be inferred that dynamic crack would grow solely driven by stress and then develop by seeking an advantageous position. However, the fractal dimension gradually increased when cracks increased and coalesced under a higher impact. This situation clearly cannot result from the gradual increase of crack roughness. As shown in the trend of crack area for S4, the crack area gradually increased with the change in slice number, corresponding to the trend of fractal dimension for S4. Therefore, when cracks develop under a higher impact, the crack network becomes more complex along the impact direction.

Fig. 14 depicts the crack development in relation to the original pores. The red and green objects were original pores, with red representing overlapping pores along the crack growth path and green indicating non-overlapping pores. According to results in Section 4.2, the crack would preferentially grow and coalesce in the area with more pores. On the condition that the crack network becomes more complex along the impact direction, exploring the relation between crack development and pores in rock is meaningful. Not all original pores were involved in the crack growth within the crack coalescence area. Three relations can be identified. The first was that crack grew next to pores, so the pores were adjacent to crack. The second was that cracks grew along pores

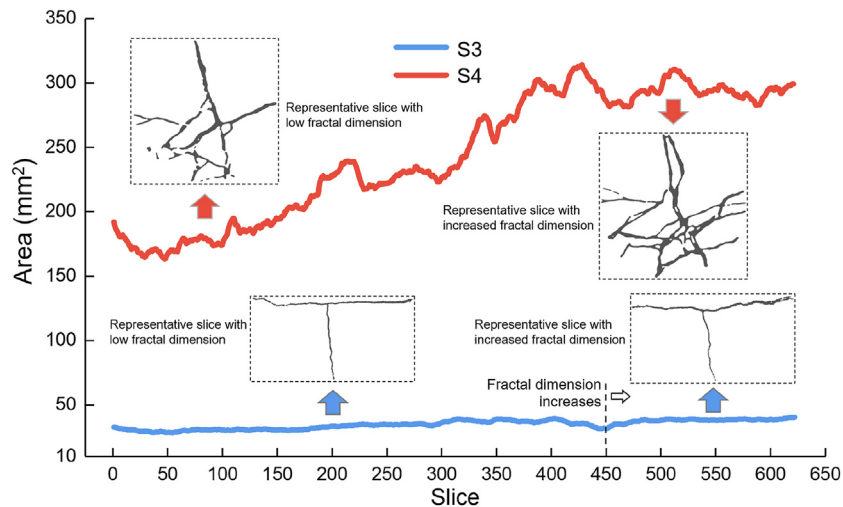


Fig. 13. Crack area of the cross-section as the slice number changes.

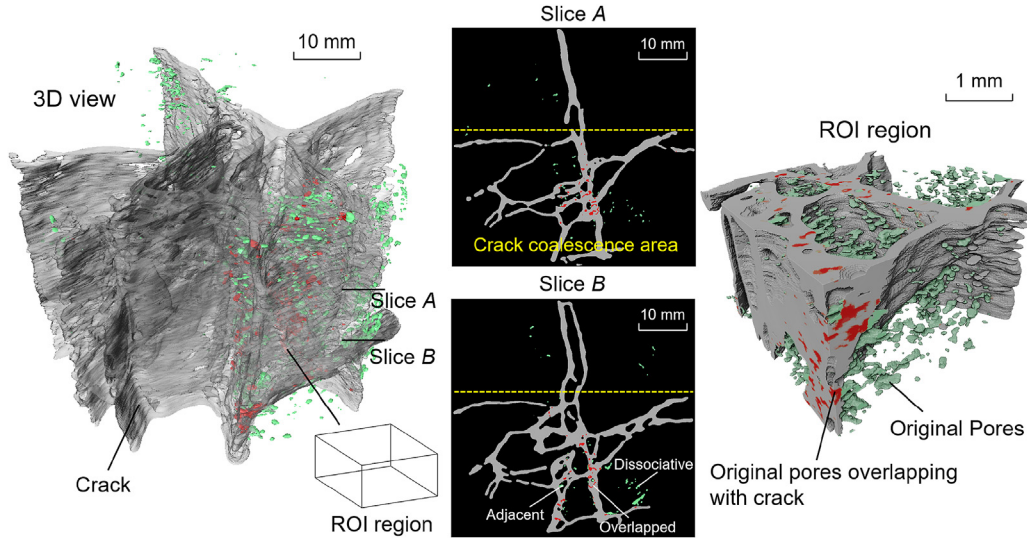


Fig. 14. Relation between crack development and original pores.

which were overlapped. The last was that the pores were located away from crack, and these pores were defined as dissociative pores. Therefore, only overlapped pores participated in the crack development. In the crack coalescence area, the volume proportion of overlapped pores to the original pores was 32%, suggesting that around a third of the pores were involved in the crack development.

Further, the percentage variation of overlapped pores was calculated as the slice changed from the top to bottom. As shown in Fig. 15, the percentage fluctuated within a wide range. An upward trend emerged as the slice number increased, and the maximum value was 62.6%, which was in the middle of the sample. The minimum was 5.98%, and small proportions could be observed at both ends. Overall, the contribution of pores to crack development generally increased along the impact direction, and the maximum position was in the middle.

5.3. Rock grains and fragments generation mechanism

The generation of rock grains and fragments is an important characteristic of rock dynamic failure. In Section 4.3, rock grains were found within cracks, and they significantly increased with

increasing impact loading. To explore the generation mechanism of rock grains and fragments, a high-resolution scanning as fine as 8 μm was conducted inside the broken sample. Fig. 16a shows the overview scanning result. A broken rock column was constructed with a height of 16.84 mm and a radius of 16.45 mm. The characteristic slice shown in Fig. 16b shows that most rock grains and fragments are detached and freely filled in cracks. However, two positions with star signs are noteworthy. First, in region A, a rock fragment with the major axis length of 2.76 mm was detached but closely clung to the rock block. Some smaller rock grains and fragments could be found within the microcrack. As shown in Fig. 16c, an around 0.16-mm wide microcrack detached the fragment from its mother block, and some smaller rock grains and fragments filled in. This situation occurred near a crack of about 1.44 mm in width. Along this crack downward (see Fig. 16b), in region B, the microcrack did not completely peel the fragment off, nor smaller grains existed therein. As shown in Fig. 16d, a 0.09-mm wide microcrack developed near a 0.783-mm wide crack.

The similarities and differences between the two cases demonstrate the microscopic properties of the dynamic crack development and the formation mechanism of rock grains and

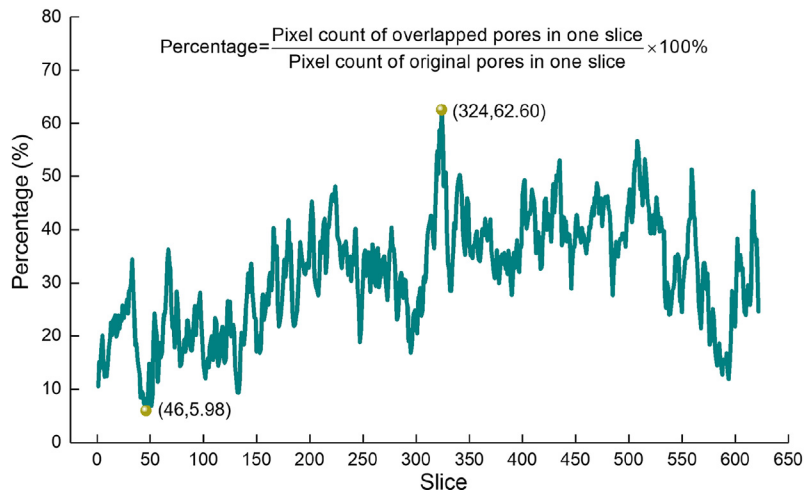


Fig. 15. Percentage variation of overlapped pores in crack coalescence area.

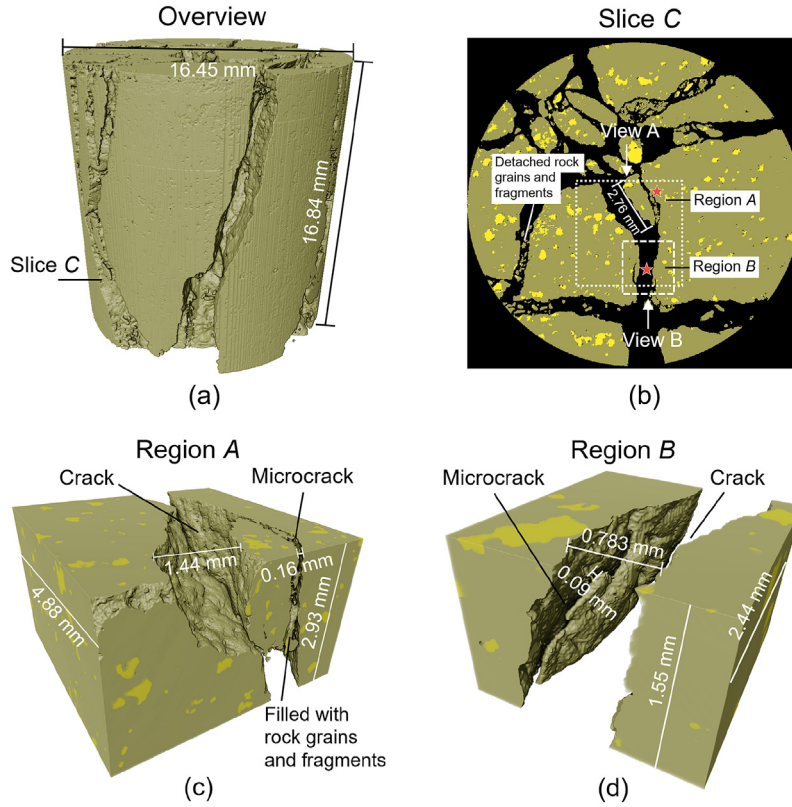


Fig. 16. Internal high-resolution scanning of a broken sample. (a) Overview, (b) slice C, (c) region A, and (d) region B.

fragments. First, the dynamic crack development accompanies by microcracks formed along its path. These microcracks can be surrounded by the other microcracks, and the formed microcrack loops result in the generation of rock grains and fragments. Here are two situations. As shown in Fig. 17a, when microcrack arrests, rock grains and fragments are in the initiation stage, where close loops do not form between the microcrack and the crack. Fig. 17c shows the actual scene, in which cracks are depicted according to region B (Fig. 16d). If the microcrack continues to develop, a close loop forms and rock grain or fragment generates. As shown in

Fig. 17b, the microcracks can be developed in multilevel. New microcracks may initiate from the microcrack that stems from crack. Close loops in rock block therefore collect, and smaller rock grains or fragments generate, as shown in Fig. 17d, which was corresponding to the case in region A (see Fig. 16c).

5.4. Native defect influence

Results show that the native defect influences the stress transfer. To understand this influence, Fig. 18 summarizes the variations

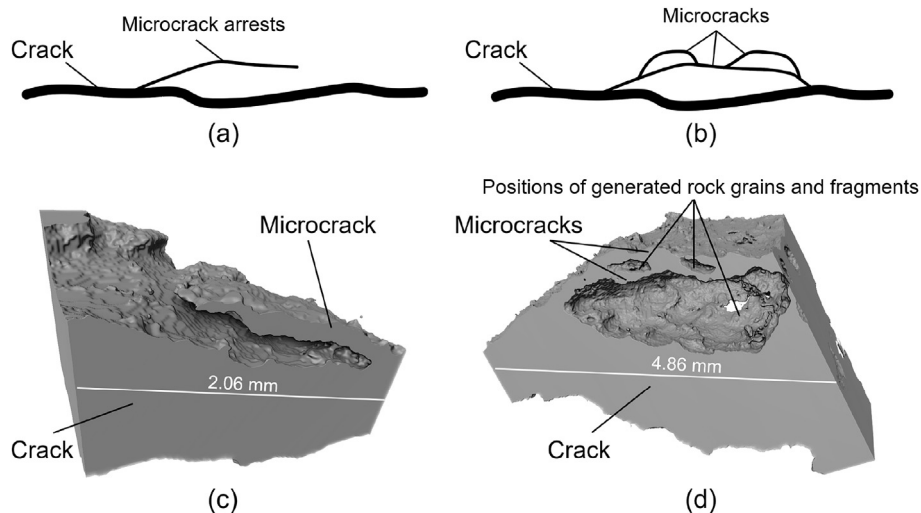


Fig. 17. Schematic diagram of rock grains and fragments generation. (a) Initiation stage, (b) generation stage, (c) scenario of region B, and (d) scenario of region A.

of crack area and fractal dimension for S5 as its slice number changes. Three zones can be identified relative to the position of initial defect. Above the defect (zone I), the crack area and the fractal dimension change smoothly, and their averages are 352.56 mm^2 and 1.43, respectively. In zone II, influenced by the initial defect, the crack area and fractal dimension both climb and then decline. They tend to be stable below the defect (zone III), and the averages are 237.29 mm^2 and 1.34, respectively. First, the averages of zone I are clearly greater than those of zone III, which indicates that the defect effectively reduces the complexity and extent of dynamic cracks. Additionally, although the two curves present a similar trend, their peaks appear in different positions.

Therefore, four characteristic slices are selected, as shown in Fig. 19. The differences between slice 26 and slice 378 intuitively illustrate the defect influence. Slices 80 and 124 are the two peak locations of the fractal dimension and the crack area, respectively. Compared to slice 124, more rock grains generate and fill in cracks, leading to a more complex crack network and a decreased crack area.

Meanwhile, the initial defect fractured throughout the sample though it was initially not. This phenomenon was due to the compression-shear effect. Fig. 20 compares the defect before and after the impact. The upper half shows the original state. The defect was initially discontinuous and exhibited an apparent roughness as it expanded outward from the upside to the downside. The lower half displayed the failure state at the defect, contrasting with the original state. From the upside to the downside, crushing failure occurred at the defect and expanded to the whole plane. The white dashed lines can help trace this change.

Based on the above analysis, a Lagrangian diagram is depicted to illustrate the propagation of the stress wavefront, as shown in Fig. 21. From the incident end to the transmitted end, the region can be divided into two zones and three stages. The first zone in red shows that the stress wave is repeatedly reflected between the upper bound and the defect. Multiple reflections lead to severer damage. The crack inside would be characterized by tensile-shear failure, as shown in Section 5.1. At the defect, compressive effect plays a critical role. Compressive-shear failure dominates, and the compression drives the shear. Afterward, the stress wavefront propagates beyond the defect. The energy carried by the stress wave has been largely dissipated. Less failure is in the second zone

in green. The reflection of the stress wave is also limited, far less than that in the first zone. The failure is back to the tensile-shear effect. Therefore, during this course, the three stages are tensile-shear failure above the defect, compressive-shear failure at the defect, and tensile-shear failure below the defect. A transformation occurs from tensile-shear to compressive-shear and then returns to tensile-shear failure.

5.5. Implications to rock engineering

Rock engineering inevitably deals with the dynamic behaviors of rock in response to geological and engineering processes, involving but not limited to the design, construction, and maintenance in various practices such as tunneling, mining, and slope engineering. Based on the results and discussions, some implications are provided to help engineers and geologists better understand and cope with the dynamic behavior of rock.

First, the findings provide the basis for tunnel or roadway supports. Rock grains and fragments filled in cracks can cause the permanent deformation of surrounding rock, and it would be more evident as the impact levels up, especially the occurrence of the rock fragments. Timely high-strength support is therefore necessary. At the same time, while taking active support or grouting measures, removing those rock grains is worth considering. Additionally, crack coalescence preferentially occurs in areas with more pores. The coalescence extent becomes greater along the impact direction. Therefore, it cannot be ignored upon deep rock failure subjected to dynamic loading. The crack development analysis in Section 5.2 also sheds light on a potential method for inversion. This method could be used to deduce the load intensity by exploiting the morphology or fractal nature of dynamic cracks. The application of this potential method could be extended to various domains, such as seismic engineering.

In mining engineering, pressure-relief techniques become more important for protecting roadways from dynamic failure (Kang et al., 2010; Ranjith et al., 2017). Emerging pressure-relief technique by directional roof cutting via blast or hydraulic fracturing is proposed and promoted because of its practicality and effectiveness in the field (Liu et al., 2020a; Zhang et al., 2020a, c). The roof cutting impedes the stress transfer from the gob and thus protects the gob-side roadway (Zhang et al., 2020b, 2023). Section 5.4 gives an

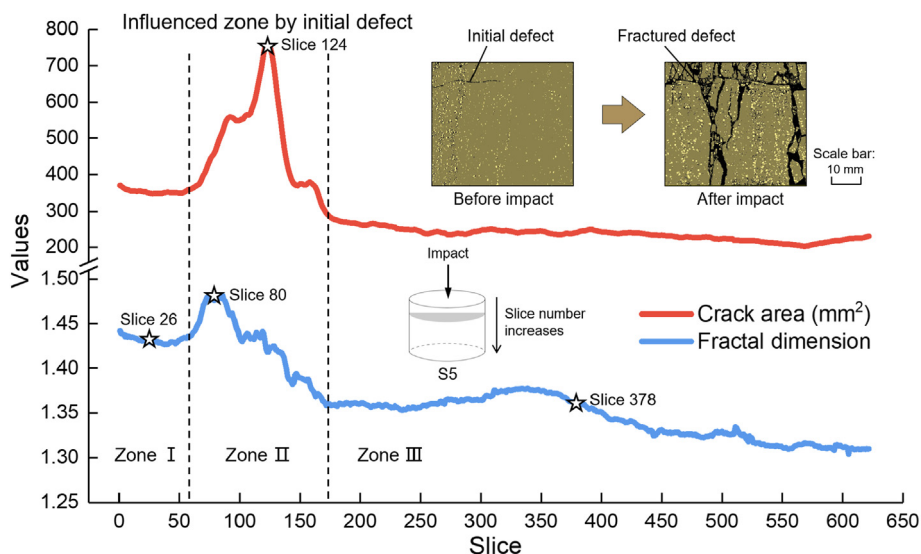


Fig. 18. Variations of crack area and fractal dimension for S5 crack slices.

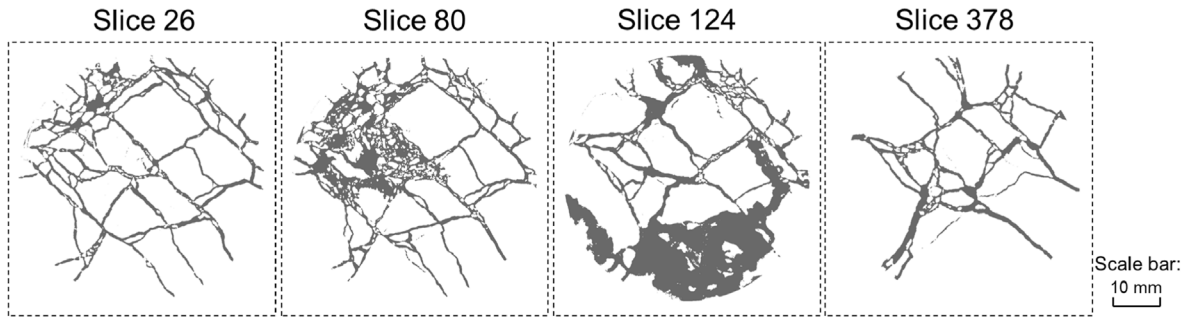


Fig. 19. Characteristic slice of crack in the cross-section view.

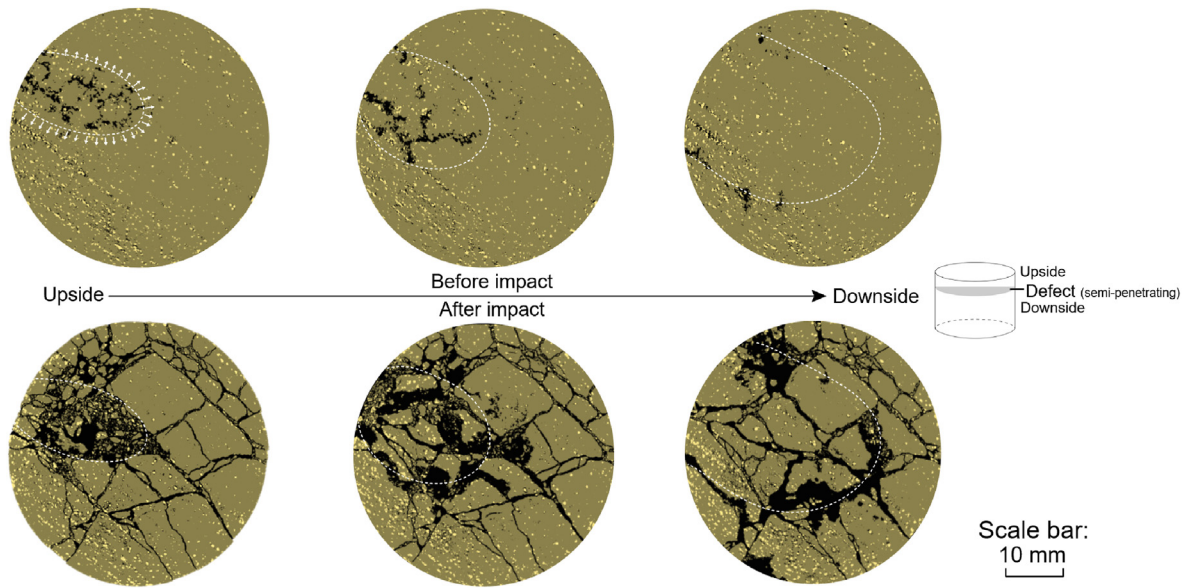


Fig. 20. Failure characteristics at the defect in the cross-section view.

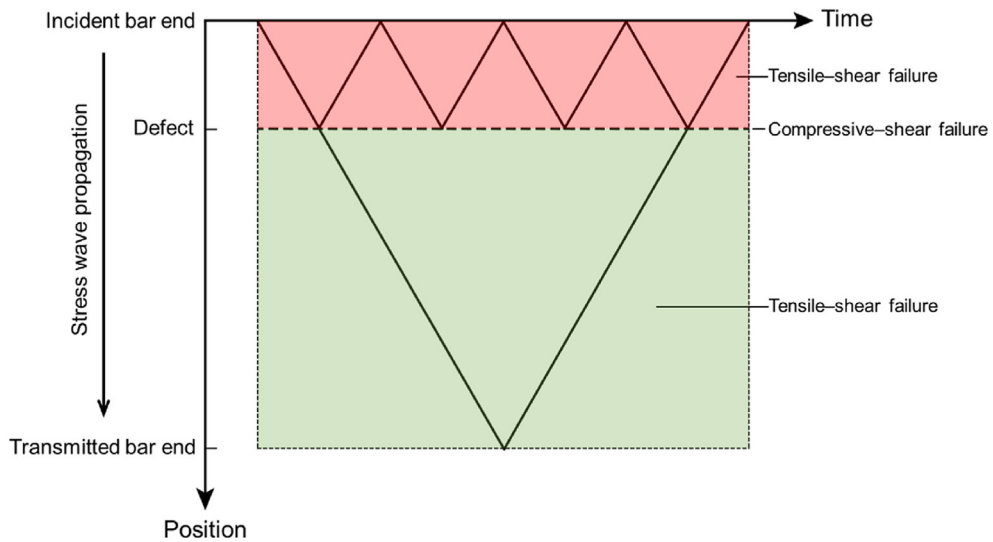


Fig. 21. Diagram for stress wave propagation and induced failure pattern in the sample with the defect.

insight that a directional defect perpendicular to the loading direction can impede stress transfer. The pressure-relief mechanism is thus verified in the laboratory experiment and observation. In addition, in slope engineering, the bedding plane serves as a weak path for rock failure (Havaej et al., 2014). This study reveals that the semi-penetrating bedding defect was transformed into a penetrating defect under impact loading. Rock above the defect was more heavily broken, and crush failure arose, accompanying a lot of rock grains and fragments at the bedding plane. The phenomena help explain some reasons for rockfall and landslides. Meanwhile, rock grains possibly decrease the shear resistance along the bedding plane, thus boosting landslide occurrence.

5.6. Remarks

Rock dynamic failure is a classic topic that has been studied extensively over recent decades (Zhang and Zhao, 2013). Many researchers have used the SHPB test to identify the strain rate dependence of impacted rock. Regardless of the rock type, it is generally agreed that the dynamic strength increases as the strain rate levels up (Zou and Wong, 2015; Li et al., 2017a). In this study, we investigated two samples under a specific impact level. Through the results in Section 4.1, we identified the dynamic strength that did not continuously increase as the strain rate increased, which has also been shown in some literature (e.g. Olsson, 1989; Qi et al., 2009; Qian et al., 2009; Wang et al., 2023). However, the reason for this phenomenon remains unclear, so we identified the initial structure of the rock samples by micro-CT pretest. We then visualized and quantified the initial structure to determine the reason behind the differences.

Furthermore, we analyzed the crack development through the digital information of dynamic cracks. The existing research has identified two main failure patterns, including simply fracturing and multiple fragmentation states, also known as split and pulverization (Doan and Gary, 2009; Braunagel and Griffith, 2019; Gong et al., 2019). However, traditional observation lies in the final crushed state of rock, while the dynamic crack information is therefore missing when the rock sample falls apart. To fill this gap, we combined the SHPB and micro-CT tests to study the microscopic failure mechanism of impacted rock. This approach allowed us to observe the internal failure, leading to the proposal of three types of dynamic cracks. We also considered the interaction between the dynamic crack development and the initial structure, as discussed in Sections 4.2, 5.2, and 5.4.

Noteworthy, we obtained the result of the sample with a natural semi-transverse defect. Therefore, we could compare different failure situations above, at, and below the defect in this context, and the defect influence and failure behaviors are discussed in Section 5.4. While some literature has reported on the influence of preexisting cracks under dynamic loads (Zhou et al., 2022; Xie et al., 2023; Zou et al., 2023), the observations and analyses are typically based on artificial cracks rather than natural cracks with a certain roughness. As a result, we discovered the localization failure and discussed the inhibition effect on stress transfer of the defect, as well as the failure mechanism influenced by the defect. In addition, by taking advantage of the microscopic 3D observation, we found the rock grains and fragments inside the cracks and discussed the generation mechanism of these rock grains and fragments.

The above analyses and results have been rarely reported. These findings have implications for rock engineering. In addition, this study introduces a methodology for assessing the potential impacts of rock heterogeneity on cracking, while it would be exciting if the temporal relationship of cracking could be considered in further

research. Inspired by the results, we also recognize the need for more specific research in the future based on the methodology.

6. Conclusions

The dynamic behavior of rock is critical for safe engineering construction in geological environments. This study explores three-dimensional failure characteristics and microscopic failure behaviors of sandstone under impact loading. The main findings are below:

- (1) Three crack types of “I,” “Y,” and “H” in the axial view are proposed to describe the dynamic crack development of rock. As the strain rate increases, the I-type crack dominates, and a transition from I- to Y- and H-type crack rises when the secondary fracture occurs. The primary fracture relies on tensile failure, while the secondary fracture results from shear failure.
- (2) When rock is simply fractured along the impact direction, crack grows irregularly. The crack area keeps stable while the fractal dimension lifts in later crack growth, during which the crack roughness increases. This is different from the situation of crack coalescence, in which the crack area and fractal dimension generally increase simultaneously. Crack network would be more complex along the impact direction.
- (3) Dynamical crack coalescence gives priority to the area where more pores preexist. Not all pores are involved in the crack development. There are also pores adjacent to cracks and dissociative pores. In this study, the volume of initial pores overlapped with the developed cracks accounted for 32%. The contribution of overlapped pores generally increased along the impact direction, and the maximum lay in the middle of sample with a value of 62.6%.
- (4) During the dynamic failure, rock grains and fragments fill in cracks, and microcracks develop in blocks. As the strain rate increases, the number of rock grains and fragments increases while microcracks initially increase and then decrease. The development of microcracks is a root of the generation of rock grains and fragments. Microcracks grow along the dynamic cracks. When the close loops form, rock grains and fragments generate. This pattern can be multilevel because new microcracks can derive from the microcrack.
- (5) The initial defect perpendicular to the loading can alter the stress-transfer form. Areas beyond the defect are characterized by tensile-shear failure while compressive-shear failure at the defect. Crushing failure occurs at the defect, and the defect develops from semi-penetrating into a penetrating fracture. As a result, the maximums of crack area and fractal dimension are in the defect-influence zone but with different locations. Along the impact direction, the rock above the defect would be damaged more severely than below. The defect shows an effect of impeding stress transfer and consuming impact energy.

CRedit authorship contribution statement

Xingyu Zhang: Project administration, Conceptualization, Data curation, Formal analysis, Funding acquisition, Investigation, Methodology, Resources, Validation, Visualization, Writing – original draft, Writing – review & editing. **Pengfei Guo:** Data curation, Funding acquisition, Methodology, Resources, Validation. **Xiangbo Gao:** Investigation, Validation, Visualization. **Chunjiang Zou:** Investigation, Validation, Writing – review & editing. **Kaiyu Wang:**

Formal analysis, Visualization. **Jin Zhu Hu:** Data curation, Formal analysis. **Yan Sun:** Data curation, Investigation, Validation. **Liang Lei:** Conceptualization, Funding acquisition, Methodology, Project administration, Writing – review & editing, Resources, Supervision.

Declaration of competing interest

The authors declare that they have no known competing financial interests or personal relationships that could have appeared to influence the work reported in this paper.

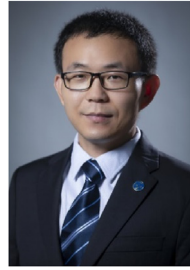
Acknowledgments

This work is supported by Research Center for Industries of the Future (RCIF), Key Laboratory of Rock Mechanics and Geohazards of Zhejiang Province (No. ZJRMG-2022-03), and Key Research and Development Program of Guangxi Province (No. Guike AB22080035), which are gratefully acknowledged. In addition, we are grateful for the valuable and constructive feedback provided by the anonymous reviewers, which has greatly improved this manuscript.

References

- Austrheim, H., Dunkel, K.G., Plümper, O., Ildefonse, B., Liu, Y., Jamtveit, B., 2017. Fragmentation of wall rock garnets during deep crustal earthquakes. *Sci. Adv.* 3, e1602067.
- Berg, S., Kutra, D., Kroeger, T., Straehle, C.N., Kausler, B.X., Haubold, C., et al., 2019. Ilastik: interactive machine learning for (bio) image analysis. *Nat. Methods* 16 (12), 1226–1232.
- Braunagel, M.J., Griffith, W.A., 2019. The effect of dynamic stress cycling on the compressive strength of rocks. *Geophys. Res. Lett.* 46, 6479–6486.
- Brown, C., Liebovitch, L., 2010. *Fractal Analysis*, first ed. Sage, New York, NY, USA.
- Brown, S.R., 1987. A note on the description of surface roughness using fractal dimension. *Geophys. Res. Lett.* 14 (11), 1095–1098.
- Changani, H., 2015. Porosity and Moisture Effects on Dynamic Strength of Two Sandstones from Utah. The University of Utah, Salt Lake City, UT, USA. MSc Thesis.
- Dai, F., Huang, S., Xia, K., Tan, Z., 2010. Some fundamental issues in dynamic compression and tension tests of rocks using split Hopkinson pressure bar. *Rock Mech. Rock Eng.* 43, 657–666.
- Doan, M.L., Gary, G., 2009. Rock pulverization at high strain rate near the San Andreas fault. *Nat. Geosci.* 2, 709–712.
- Emad, M., Waqas, M., Khan, M., 2023. Investigating the impacts of porosity on the rock mechanical properties of sandstone. In: *The ARMA US Rock Mechanics/ Geomechanics Symposium*, ARMA-2023-0578.
- Falconer, K., 2007. *Fractal Geometry: Mathematical Foundations and Applications*. John Wiley & Sons.
- Gong, F.Q., Si, X.F., Li, X.B., Wang, S.Y., 2019. Dynamic triaxial compression tests on sandstone at high strain rates and low confining pressures with split Hopkinson pressure bar. *Int. J. Rock Mech. Min. Sci.* 113, 211–219.
- Havaej, M., Stead, D., Eberhardt, E., Fisher, B.R., 2014. Characterization of bi-planar and ploughing failure mechanisms in footwall slopes using numerical modelling. *Eng. Geol.* 178, 109–120.
- Huang, S., Xia, K., Zheng, H., 2013. Observation of microscopic damage accumulation in brittle solids subjected to dynamic compressive loading. *Rev. Sci. Instrum.* 84, 093903.
- Kang, H., Zhang, X., Si, L., Wu, Y., Gao, F., 2010. In-situ stress measurements and stress distribution characteristics in underground coal mines in China. *Eng. Geol.* 116, 333–345.
- Katcoff, C.Z., Graham-Brady, L.L., 2014. Modeling dynamic brittle behavior of materials with circular flaws or pores. *Int. J. Solid Struct.* 51 (3–4), 754–766.
- Li, X., Gong, F., Tao, M., Dong, L., Du, K., Ma, C., Zhou, Z., Yin, T., 2017a. Failure mechanism and coupled static-dynamic loading theory in deep hard rock mining: a review. *J. Rock Mech. Geotech. Eng.* 9, 767–782.
- Li, X., Li, H., Liu, K., Zhang, Q., Zou, F., Huang, L., Zhao, J., 2017b. Dynamic properties and fracture characteristics of rocks subject to impact loading. *Chin. J. Rock Mech. Eng.* 36, 2393–2405.
- Li, X., Zou, Y., Zhou, Z., 2013. Numerical simulation of the rock SHPB test with a special shape striker based on the discrete element method. *Rock Mech. Rock Eng.* 47, 1693–1709.
- Liang, S., Wu, S., Li, S., Liu, D., Wu, R., 2015. Study on the determination of specimen size in SHPB experiments of rock materials. *Eng. Blast.* 21, 1–5.
- Liu, J., Liu, C., Yao, Q., Si, G., 2020a. The position of hydraulic fracturing to initiate vertical fractures in hard hanging roof for stress relief. *Int. J. Rock Mech. Min. Sci.* 132, 104328.
- Liu, K., Zhang, Q., Wu, G., Li, J., Zhao, J., 2019. Dynamic mechanical and fracture behaviour of sandstone under multiaxial loads using a triaxial Hopkinson bar. *Rock Mech. Rock Eng.* 52, 2175–2195.
- Liu, K., Zhang, Q., Zhao, J., 2018. Dynamic increase factors of rock strength. In: *Rock Dynamics – Experiments, Theories and Applications*. Taylor & Francis Group, pp. 169–174.
- Liu, K., Zhao, J., Wu, G., Maksimenko, A., Haque, A., Zhang, Q., 2020b. Dynamic strength and failure modes of sandstone under biaxial compression. *Int. J. Rock Mech. Min. Sci.* 128, 104260.
- Luo, Y., Wang, G., Li, X., Liu, T., Mandal, K., Xu, M., Xu, K., 2020. Analysis of energy dissipation and crack evolution law of sandstone under impact load. *Int. J. Rock Mech. Min. Sci.* 132, 104359.
- Ma, Z., He, X., Kwak, H., Gao, J., Sun, S., Yan, B., 2023a. Enhancing rock image segmentation in digital rock physics: a fusion of generative AI and state-of-the-art neural networks. *arXiv preprint arXiv:2311.06079*.
- Ma, Z., He, X., Sun, S., Yan, B., Kwak, H., Gao, J., 2023b. Zero-shot Digital Rock Image Segmentation with a Fine-Tuned Segment Anything Model *arXiv preprint arXiv:2311.10865*.
- Misa, R., Nowakowski, A., 2021. Comparison of the compressive and tensile strength values of rocks obtained on the basis of various standards and recommendations. *Symmetry* 13 (7), 1163.
- Mishra, S., Chakraborty, T., Basu, D., Lam, N., 2020. Characterization of sandstone for application in blast analysis of tunnel. *Geotech. Test J.* 43 (2), 351–382.
- Olsson, W.A., 1989. The Effect of Strain Rate on the Compressive Strength of Dry and Saturated Tuff. Sandia National Laboratories, Albuquerque, NM, USA.
- Padmanabha, V., Schäfer, F., Rae, A.S.P., Kenkmann, T., 2023. Dynamic split tensile strength of basalt, granite, marble and sandstone: strain rate dependency and fragmentation. *Rock Mech. Rock Eng.* 56 (1), 109–128.
- Purswani, P., Karpyn, Z.T., Enab, K., Xue, Y., Huang, X., 2020. Evaluation of image segmentation techniques for image-based rock property estimation. *J. Pet. Sci. Eng.* 195, 107890.
- Qi, C., Wang, M., Qian, Q., 2009. Strain-rate effects on the strength and fragmentation size of rocks. *Int. J. Impact Eng.* 36, 1355–1364.
- Qian, Q., Qi, C., Wang, M., 2009. Dynamic strength of rocks and physical nature of rock strength. *J. Rock Mech. Geotech. Eng.* 1, 1–10.
- Ranjith, P.G., Zhao, J., Ju, M., De Silva, R.V.S., Rathnaweera, T.D., Bandara, A.K.M.S., 2017. Opportunities and challenges in deep mining: a brief review. *Eng. Plast.* 3, 546–551.
- Reinhardt, M., Jacob, A., Sadeghnejad, S., Cappuccio, F., Arnold, P., Frank, S., et al., 2022. Benchmarking conventional and machine learning segmentation techniques for digital rock physics analysis of fractured rocks. *Environ. Earth Sci.* 81 (3), 71.
- Saouma, V.E., Barton, C.C., Gamaleldin, N.A., 1990. Fractal characterization of fracture surfaces in concrete. *Eng. Fract. Mech.* 35, 47–53.
- Sun, B., Liu, S., Zeng, S., Wang, S., Wang, S., 2021. Dynamic characteristics and fractal representations of crack propagation of rock with different fissures under multiple impact loadings. *Sci. Rep.* 11, 13071.
- Wang, G.Y., Yu, R., Ma, D.F., Wang, X.Y., Cao, A.S., Hou, Y., Ren, L.W., 2022. Failure characteristics and failure process investigation of fine-grained sandstone under impact load by ultrahigh speed DIC and SEM techniques. *Int. J. GeoMech.* 22 (7), 04022108.
- Wang, P., Xu, J., Liu, S., Wang, H., 2016. Dynamic mechanical properties and deterioration of red-sandstone subjected to repeated thermal shocks. *Eng. Geol.* 212, 44–52.
- Wang, Z., Huang, J., Chen, Y., Li, X., Liu, T., Meng, F., 2023. Dynamic mechanical properties of different types of rocks under impact loading. *Sci. Rep.* 13, 19147.
- Wen, T., Cheong, K.H., 2021. The fractal dimension of complex networks: a review. *Inf. Fusion* 73, 87–102.
- Xie, H., Wang, J., Xie, W., 1997. Fractal effects of surface roughness on the mechanical behavior of rock joints. *Chaos, Solit. Fractals* 8, 221–252.
- Xie, X., Li, J., Zheng, Y., 2023. Experimental study on dynamic mechanical and failure behavior of a jointed rock mass. *Int. J. Rock Mech. Min. Sci.* 168, 105415.
- Yao, W., Xu, Y., Xia, K., 2020. Damage evolution during rock pulverization induced by dynamic compressive loading. *J. Geophys. Res. Solid Earth* 125 (5), e2020JB019388.
- Zhang, Q.B., Zhao, J., 2013. A review of dynamic experimental techniques and mechanical behaviour of rock materials. *Rock Mech. Rock Eng.* 47, 1411–1478.
- Zhang, X., He, M., Yang, J., Wang, E., Zhang, J., Sun, Y., 2020a. An innovative non-pillar coal-mining technology with automatically formed entry: a case study. *Eng. Plast.* 6, 1315–1329.
- Zhang, X., Hu, J., Xue, H., Mao, W., Gao, Y., Yang, J., He, M., 2020b. Innovative approach based on roof cutting by energy-gathering blasting for protecting roadways in coal mines. *Tunn. Undergr. Space Technol.* 99, 103387.
- Zhang, X., Pak, R.Y.S., Gao, Y., Liu, C., Zhang, C., Yang, J., He, M., 2020c. Field experiment on directional roof presplitting for pressure relief of retained roadways. *Int. J. Rock Mech. Min. Sci.* 134, 104436.
- Zhang, X., Pak, R.Y.S., Yang, J., Lei, L., Niu, H., Niu, Y., Zhao, C., Gao, H., He, M., 2023. Mechanistic formulation and validation of cutting seam by energy-focusing blast for pressure relief of deep roadway. *Eng. Fail. Anal.* 150, 107378.
- Zhao, J., Li, J., 2013. *Rock Dynamics and Applications-State of the Art*, first ed. CRC Press, Boca Raton, FL, USA.
- Zhou, T., Han, Z., Li, D., Chen, J., 2022. Experimental study of the mechanical and

- fracture behavior of flawed sandstone subjected to coupled static-repetitive impact loading. *Theor. Appl. Fract. Mech.* 117, 103161.
- Zhou, Y., Xia, K., Li, X., Li, H., Ma, G., Zhao, J., Zhou, Z., Dai, F., 2012. Suggested methods for determining the dynamic strength parameters and mode-I fracture toughness of rock materials. *Int. J. Rock Mech. Min. Sci.* 49, 105–112.
- Zhou, Z., Cai, X., Li, X., Cao, W., Du, X., 2019. Dynamic response and energy evolution of sandstone under coupled static-dynamic compression: insights from experimental study into deep rock engineering applications. *Rock Mech. Rock Eng.* 53, 1305–1331.
- Zou, C., Li, J., Liu, K., Zhao, X., 2023. Dynamic cracking process of rock interpreted by localized strain-rate, rate-dependent strength field and transition strain-rate. *Int. J. Rock Mech. Min. Sci.* 163, 105340.
- Zou, C., Wong, L.N.Y., 2015. Size and geometry effects on the mechanical properties of Carrara Marble under dynamic loadings. *Rock Mech. Rock Eng.* 49, 1695–1708.



Dr. Liang Lei joined Westlake University in 2020 as an assistant professor after three years of postdoctoral research at the National Energy Technology Laboratory in the U.S. He obtained his BSc in 2009 and MSc in 2012 from Tongji University, and PhD in 2017 from Georgia Institute of Technology. His lab, Digital Porous Media Laboratory, focuses on multi-physics and phase transformation processes in porous media targeting energy and earth science-oriented problems. Featured techniques include in situ experiments based on micro-CT and in-depth analysis based on 3D sample internal structure. He is the recipient of the best reviewer award from the journal of *Geomechanics for Energy and the Environment*, the best paper award in 2021 from the journal of *Marine and Petroleum Geology*, and the 2021 Faculty Award of Excellence in Teaching from the SoE, Westlake University. He is also a scientific editor of *Journal of Rock Mechanics and Geotechnical Engineering* (JRMGE).